# Enhancement of the Field Emission from the TiO₂ Nanotube Arrays by Reducing in a NaBH₄ Solution

Xuqiang Zhang, Chengwei Wang,* Jianbiao Chen, Weidong Zhu, Aizhen Liao, Yan Li, Jian Wang, and Li Ma

Key Laboratory of Atomic and Molecular Physics & Functional Materials of Gansu Province, College of Physics and Electronic Engineering, Northwest Normal University, Lanzhou 730070, China

ABSTRACT: A mass of oxygen vacancies are successfully introduced into TiO_2 nanotube arrays using low-cost $NaBH_4$ as a reductant in a liquid-phase environment. By controlling and adjusting the reduction time over the range of 0−24 h, the doping concentration of the oxygen vacancy is controllable and eventually reaches saturation. Meanwhile, the thermal stability of oxygen vacancies is also investigated, indicating that part of the oxygen vacancies remain stable up to 250 °C. In addition, this liquid-phase reduction strategy significantly lowers the requirements of instruments and cost. More interesting, reduced TiO_2 nanotube arrays show drastically enhanced field emission performances including substantially decreased turn-on field from 25.01 to 2.65 V/μm, a high current density of 3.5 mA/cm² at 7.2 V/μm, and an excellent field emission stability and repeatability. These results are attributed to the oxygen vacancies obtained by reducing in $NaBH_4$ solution, resulting in a reduced effective work function and an increased conductivity.

KEYWORDS: field emission, TiO₂ nanotube, oxygen vacancy, effective work function, conductivity
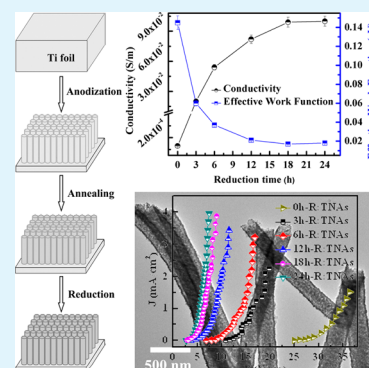
INTRODUCTION

Because of their unique properties of surface morphology, large current-carrying capacity, and good mechanical strength, one-dimensional (1D) nanomaterials have found numerous applications,[1−7] especially being hailed as charming candidates for field emitters owing to their high aspect ratio and sharp tips. As one of the most important 1D nanomaterials, carbon nanotubes (CNTs) seem to be the most hopeful field emission (FE) material.[7−9] Unluckily, they could quickly degrade under the low vacuum condition because of easy oxidation and ablation, which impedes their practical application in field emission devices.[8,9] To solve this problem, various 1D metal oxide nanomaterials, including TiO_2,[1−3] SnO_2,[4] Fe_2O_3,[5] and ZnO[6] with nanotube, nanorod, and nanowire morphologies, have been extensively studied for extending the field emitter candidates due to their superior antioxidation ability, which can work steadily under the circumstance of low vacuum or relatively high oxygen partial pressure.[10] Among various 1D metal oxide nanomaterials, TiO_2 nanotube arrays (TNAs) fabricated by anodization possess their own advantages, such as a lower work function (4.5 eV), superior electrical contact, and simple preparation method.[1,3,9] However, up to this point, TNAs have not satisfied all the requirements for practical application in FE. There are still some basic obstacles to overcome, including a slightly high turn-on field and relatively low emission current density resulting from their low conductivity and high electron affinity.[1,3,11]

A wealth of studies have been focused on enhancing the FE performances of TNAs by element doping such as N,[12] C,[13] and Fe,[14] which can create additional energy levels within the band gap of TNAs so that this method could improve the conductivity and decrease the actual work function. For example, Liu et al.[12] found that the nitrogen-doped TNAs have a lower turn-on field (11.2 V/μm). The carbon-doped TNAs also can substantially reduce the turn-on field to 5.0 V/μm and improve their FE performances.[13] However, the solubility of doped ions is usually low and doping may cause undesired structures in TNAs, as well as characterization alteration, so the turn-on field and emission current density still remain insufficient compared with CNT (turn-on field about 0.98 V/μm)[8] and metal oxide nanomaterial[15,16] based FE research. Recently, reduced TiO_2 nanotube arrays (R:TNAs) which contain Ti^{3+} or oxygen vacancies have attracted increasing interest in water splitting, photocatalysts, and fuel cells owing to their additional properties compared with pure TiO_2, including narrow band gap and high electrical conductivity.[17,18] The oxygen vacancies are shallow donors and play an important role in determining the electronic properties of TiO_2.[18] Moreover, both experimental and theoretical research has found that the metal oxides with more-reduced forms have lower actual work functions compared with oxidized forms.[19,20] Hence, it is expected that reduction treatment of TNAs can also substantially decrease their actual work function and increase their conductivity so that the FE performances of TNAs are enhanced.
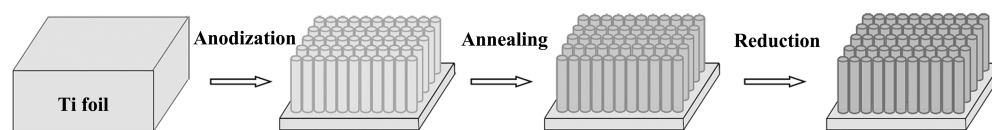
Figure 1. Schematic diagram displaying the preparation of *t*-R:TNAs (*t* = 0, 3, 6, 12, 18, and 24 h).

To obtain R:TNAs, various methods including hydrogenation, thermal reduction, and high energy laser ablation have been reported.[9,21,22] For instance, in our previous works the TNAs were reduced using high-purity hydrogen or solid NaBH₄ as reducing agents.[9,21] Although the reduction strategies could introduce an amount of oxygen vacancies into TNAs, the experimental process usually required multiple steps, higher temperature, longer time, special apparatus, and rigorous conditions, which limits their practical application. Moreover, the high-quality tubular structure is difficult to be obtained, because these strategies in turn cause damage of nanotubes or compositional inhomogeneity. Therefore, developing an economical and uncomplicated method to synthesize the R:TNAs is still a great challenge. Recently, Xing et al.[23] found that the reduced TiO₂ nanopaticles were successfully synthesized using a strong reducing reagent NaBH₄ at a lower temperature in a liquid-phase environment. During the hydrothermal process, NaBH₄ can easily hydrolyze and release the reductive H₂ and atomic hydrogen:

$$8Ti^{4+} + NaBH_4 + 2H_2 \rightarrow 8Ti^{3+} + NaBO_2 + 8H^+ \quad (1)$$
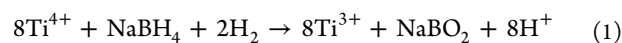
In this reducing condition, the reduction of Ti⁴⁺ is facilitated by atomic hydrogen and generates Ti³⁺,[23] which can improve the conductivity. Consequently, it is expected that the NaBH₄ liquid-phase treatment may be a useful way to reduce the preparation cost and enhance the FE performances of TNAs. To our knowledge, the corresponding FE study has not been reported elsewhere.

In this work, the R:TNAs are prepared by a simple liquid-phase reduction at 30 °C in the NaBH₄ solution, instead of as in our previous work,[21] where the TNAs were reduced by using the NaBH₄ solid-phase thermal reduction in argon atmosphere at 340−400 °C for 20 h in a tube furnace. This reduction strategy not only significantly reduces the requirements of the instruments and cost compared to the conventional strategies but also realizes controllable doping of oxygen vacancies. Moreover, in the range of 0−250 °C, the oxygen vacancies of the sample show superior thermal stability. More importantly, compared with the pristine TNAs, the R:TNAs possess higher conductivity and lower effective work function; thus, FE performances are improved. As a result, by adjusting the reduction time ranging from 0 to 24 h, the FE properties of R:TNAs are substantially improved, including low turn-on field (2.65 V/μm) and remarkable FE stability and repeatability.

■ EXPERIMENTAL SECTION

The fabrication method of TNAs was similar to that used in our previous report.[9] The following describes in detail the fabrication strategy of R:TNAs. As-prepared TNAs were annealed at 450 °C for 3 h with heating and cooling rates of 3 °C min⁻¹ in air environment to improve crystallinity. Then the annealed samples were dipped in a Teflon-lined stainless steel autoclave filled with 1−5 M NaBH₄ solution at 30 °C for different durations of 0, 3, 6, 12, 18, and 24 h. Compared with the conventional strategies,[9,21,22] the NaBH₄ liquid-phase reduction was more straightforward and low-cost. Due to NaBH₄ hydrolysis, which can produce large volumes of gas, the pressure of the Teflon-lined stainless steel autoclave rose sharply. If the

reducing agent concentration got too high, the instruments became insecure. Conversely, the low NaBH₄ concentration impeded the introduction of the amount of oxygen vacancy into the samples. Hence, we chose a moderate reducing agent concentration. After this reduction treatment, the specimens were rinsed with pure ethanol and deionized water, dried, and ground to obtain reduced TiO₂ nanotube arrays, which were denoted as *t*-R:TNAs, where *t* describes the time of reduction treatment (*t* = 0, 3, 6, 12, 18, and 24 h, respectively). A schematic illustration of the experimental process is also shown in Figure 1.

A FE scanning electron microscope (FESEM; ZEISS, ULTRA plus, operation at 5.0 kV) with an X-ray energy dispersive spectroscopy (EDS) analyzed the morphology of the specimens. X-ray diffraction (XRD) was used to study the structure of the nanotube arrays using a Rigaku D/max-2400 diffractometer (with Cu Kα₁ 0.154056 nm radiation at 40 kV and 150 mA). A transmission electron microscope (TEM) with corresponding selected area electron diffraction (SAED) pattern was used to analyze the microstructure and crystallinity (Tecnai-G2-F30, operation at 300 kV). Micro-Raman scattering measurements were performed at room temperature with 632.8 nm excitation (Horiba HR800 Raman system, He−Ne laser). To assess the band gap and oxygen vacancies of *t*-R:TNAs, the UV−vis absorption spectra of as-prepared specimens were recorded on a Shimadzu UV-2600 UV−vis spectrophotometer with an integrating sphere detector. The *I*−*V* curves of the specimens were measured by the 2-probe method on a Keithley 4200 semiconductor characterization system (electrode contact area of 2.56 × 10⁻⁶ m²) at room temperature in air environment. The test equipment and method of the FE properties were the same as in our previous work.[9]

■ RESULTS AND DISCUSSION

Typical FESEM images of *t*-R:TNAs treatment at various times of 0−24 h are shown in Figure 2. A pristine sample (0h-

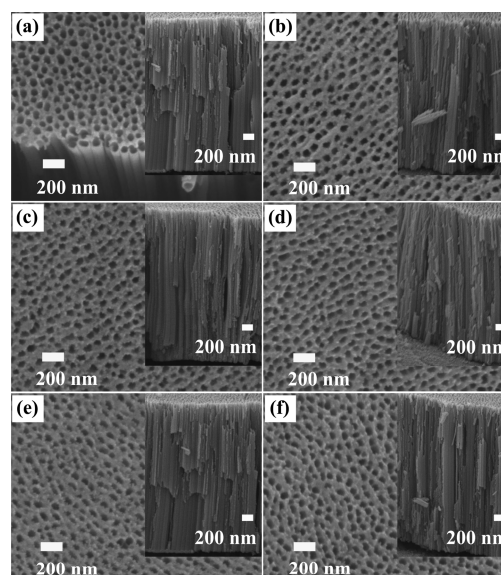**Figure 2.** (a−f) FESEM images of the *t*-R:TNAs with NaBH₄ treatment at various times (*t* = 0, 3, 6, 12, 18, and 24 h, respectively) at 30 °C; the insets of the panels show corresponding side views of samples. Scale bars: 200 nm.
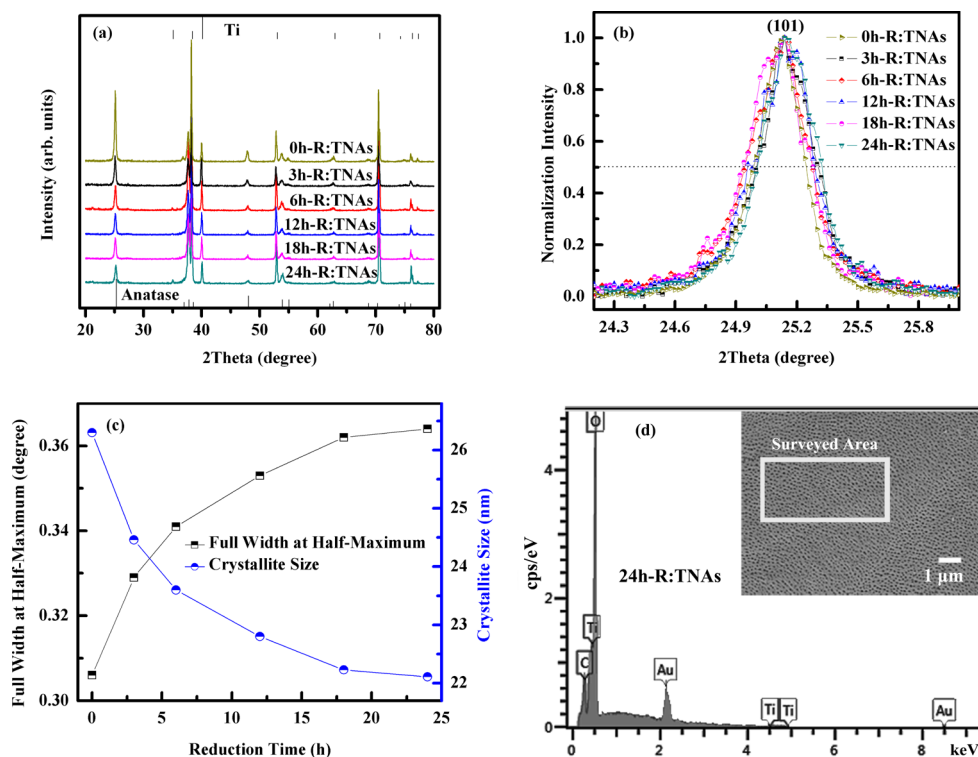
Figure 3. (a) XRD patterns of *t*-R:TNAs obtained at different reduction times. Vertical marks represent the anatase TiO$_2$ (JCPDS card 21-1272) and metallic titanium (JCPDS card 05-0682), respectively. (b) Normalized fwhm of the anatase peak (101) located at 25.28° of *t*-R:TNAs. (c) Corresponding variations of fwhm located at 25.28° and average crystallite sizes with reduction time. (d) EDS spectrum of the 24h-R:TNAs; the inset corresponds to the FESEM image.

R:TNAs) exhibits porous and uniform distribution morphology on the top with tubular structure underneath, as seen in Figure 2a and the corresponding side view. The layer thickness and density of the 0h-R:TNAs are calculated to be 3.0 μm and 2.6 × 10^9 cm^{-2}, respectively. The morphologies of R:TNAs synthesized for 3, 6, 12, 18, and 24 h are consistent with the 0h-R:TNAs (Figure 2b−f). These phenomena indicate that the NaBH$_4$ treatment has not destroyed the nanotubular structure of the samples. Because of the 1D characteristics of the nanotubes, the well-aligned TNAs vertically oriented from the Ti substrate facilitate directional charge transport.[18] The samples completely remain the electron emission sites on the top of the TNAs.

The composition, possible phase changes, and crystal structure of the samples after the NaBH$_4$ treatment are researched using the XRD and EDS techniques. All the prepared samples have an obvious anatase phase, as revealed in Figure 3a, which is similar to the standard values of bulk TiO$_2$ (JCPDS card 21-1272) besides the diffraction peaks of metallic Ti from JCPDS card 05-0682. Furthermore, with increase of reduction time, the peak intensity and the full widths at half-maximum (fwhm's) of the dominant anatase peak (101) located at 25.28° gradually weaken and broaden, respectively (Figure 3a and b). In other words, the crystallinity and average crystallite sizes of the TNAs degrade and decrease little by little after reduction, respectively. Meanwhile, as shown in Figure 3c, the mean crystallite sizes of *t*-R:TNAs are calculated to be 26.30, 24.46, 23.60, 22.80, 22.36, and 22.11 nm by the Scherrer equation,[24] respectively. Such changes, the diminished crystallite sizes and the widened fwhm of diffraction peak (101), could be attributed to the incoming oxygen vacancies.[9,25] Interestingly, in this work, these phenomena have a tendency to

saturate. This is due to the amount of the oxygen vacancy eventually attaining saturation with the increase of reduction time, which means that the improvement of NaBH$_4$ treatment lies within a limited range in this work. Moreover, the peak intensities of (004) at ~37.8° in *t*-R:TNAs have increased with the increase of reduction time, indicating NaBH$_4$ treatment restrains the growth of the (101) direction but favors the (004) direction. The EDS spectrum image taken from the 24h-R:TNAs is represented in Figure 3d, and the inset corresponds to the FESEM. It is confirmed that the sample of the reduction treatment is composed of Ti and O, indicating that it is pure titanium dioxide and similar to the XRD results. The gold and carbon signals in Figure 3d are from the spraying gold and conductive tape on the sample, respectively.

To examine the microstructure and crystallinity of the resulting R:TNAs, TEM investigation is carried out. Figure 4a and b show the different low-magnification TEM images of the 24h-R:TNAs. The nanotubes with a mean diameter of ~250 nm have a linearly and vertically oriented architecture with a rough surface. Figure 4c is a typical high-resolution TEM pattern taken from the edge of the nanotube in Figure 4b, and the corresponding selected area electron diffraction (SAED) pattern is shown in Figure 4d. The results indicate that the 24h-R:TNAs is polycrystalline, and the lattice spacing of the sample is 0.35, 0.24, and 0.19 nm, corresponding to the *d* spacing of the (101), (004), and (200) of anatase TiO$_2$,[26] respectively. These phenomena are well in agreement with the XRD patterns in Figure 3a.

Raman scattering is conducted to specifically analyze the microstructures of the samples. As shown in Figure 5, the Raman spectra of *t*-R:TNAs contain strong peaks at ~143 cm^{-1} (E$_g$), 197 cm^{-1} (E$_g$), 399 cm^{-1} (B$_{1g}$), 519 cm^{-1} (B$_{1g}$), and 639
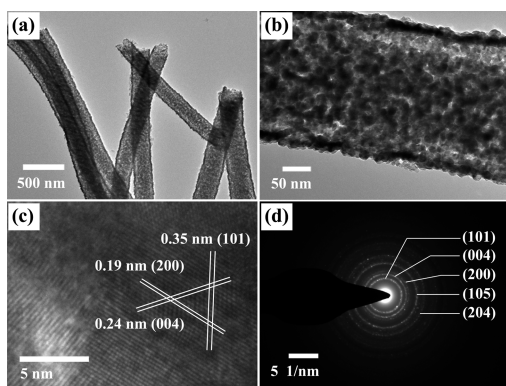
Figure 4. TEM characterization of the 24h-R:TNAs: (a) and (b) show the different low-magnification TEM images, indicating the vertically oriented nanotubes structure with a rough surface; (c) and (d) are HRTEM images and the corresponding SAED pattern of the sample, respectively, clearly showing the anatase nature.
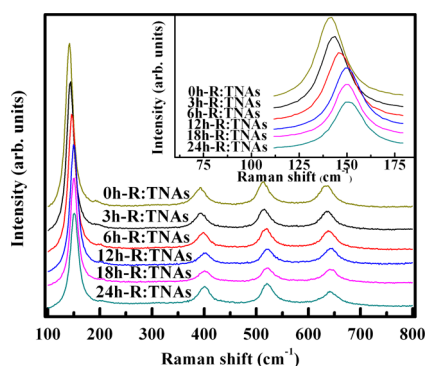

Figure 5. Raman spectra of t-R:TNAs obtained at different reduction times. Inset is the magnified view of the dominant E_g Raman mode of specimens.

cm^{-1} (E_g), indicating that the t-R:TNAs are composed of anatase TiO$_2$ structure.[21] It is worth noting that the main Raman active mode located at ~143 cm^{-1} (E_g) from t-R:TNAs shifts and broadens toward higher wavenumbers and becomes relatively more evident with the increase of reduction time, as shown in the inset of Figure 5 and Table 1. Plenty of scientific

Table 1. Wavenumbers and fwhm of the Shifted Dominant E_g Raman Mode of the t-R:TNAs

	t-R:TNAs					
samples	0 h	3 h	6 h	12 h	18 h	24 h
E_g peak (cm^{-1})	142.05	143.83	145.60	149.16	150.94	150.94
fwhm (cm^{-1})	15.56	16.35	16.61	17.26	18.22	18.39

research has found that the finite size of particles (<10 nm) or shortening of the correlation length, which is due to the presence of oxygen vacancies, would cause alterations of the lowest-frequency E_g mode.[9,17,21] Because the crystalline sizes of t-R:TNAs obtained from XRD measurement are not less than 22 nm, the only practical conclusion is that the oxygen vacancies result in the broadening and large blue-shift of the E_g mode of t-R:TNAs. Note that in the Raman scattering of the t-R:TNAs, the amount of oxygen vacancy has eventually reached

saturation with the increase of reduction time, which is also completely consistent with the XRD results.

To qualitatively describe the presence of oxygen vacancies in t-R:TNAs, the samples' UV−vis absorption spectra are investigated. As shown in Figure 6a, the absorption edges gradually shift to the visible light region with the increase of reduction time. Such phenomena can be attributed to changes in a sample's band gap. Consequently, according to Tauc's equation $\alpha h\nu = A(h\nu - Eg)^{1/2}$,[27] where A, Eg, ν, h, and α are a constant, band gap energy, light frequency, Planck's constant, and absorption coefficient, respectively, the direct band gap energies of samples are calculated using the point of intersection of the tangents to the plots of $(\alpha h\nu)^2$ vs $(h\nu)$ (in Figure 6b). The band gap energy of 0h-R:TNAs is ~3.21 eV, which is similar to the reported value of anatase TiO$_2$.[1] Interestingly, the t-R:TNAs exhibit smaller band gaps of 3.13, 3.09, 3.04, 2.99, and 2.98 eV at various reduction times of 3, 6, 12, 18, and 24 h, respectively. Such a red-shift of absorption edges and narrowed band gaps of t-R:TNAs are associated with the oxygen vacancy levels, which are located below the conduction band of TiO$_2$.[9,28] Hence, the transitions from the TiO$_2$ valence band to the oxygen vacancy levels or from the oxygen vacancies to the TiO$_2$ conduction band lead to additional energy absorbing in the visible and near-infrared light.[28] It is noticed that all of these phenomena, including the red-shift of absorption edges, narrowed band gap, and increased oxygen vacancies, have eventually reached saturation with the increase of reduction time.

The I−V characteristics of the t-R:TNAs were metered by the 2-probe method to verify the presence of oxygen vacancies after the NaBH$_4$ treatment. Figure 7a reveals the electron transport properties of the specimens; it is apparent that the currents of all t-R:TNAs gradually rise and eventually reach saturation, indicating that the reduction treatment alters the electrical performances of TNAs. Furthermore, the I−V characteristics of t-R:TNAs obtained at 0, 3, and 6 h are unsymmetrical, which due to the samples possess a Schottky barrier. In contrast, after NaBH$_4$ treatment above 12 h, the samples display an ohmic feature with symmetric graphs.[1] When the tube length and contact area are about 3.0 μm and 2.56 × 10^{-6} m^2, respectively, the conductivity values for the t-R:TNAs are calculated to be (1.32 ± 0.02) × 10^{-4}, (2.08 ± 0.03) × 10^{-2}, (5.41 ± 0.03) × 10^{-2}, (8.25 ± 0.04) × 10^{-2}, (9.98 ± 0.04) × 10^{-2}, and (1.01 ± 0.05) × 10^{-1} S/m at reduction times of 0, 3, 6, 12, 18, and 24 h (in Figure 7b), respectively. It is significant that conductivities of t-R:TNAs increase gradually with the increase of reduction time, which is a similar trend as noted for the oxygen vacancies. It is clear that the introduced oxygen vacancies in TNAs by the reduction treatment will improve the conductivity and mobility, traits essential for electronic transmission in FE applications.

The thermal stability of oxygen vacancy has to be considered as an important indicator for future applications; here a preliminary result about the thermal stability of oxygen vacancies in t-R:TNAs is presented. The 24h-R:TNAs were annealed afresh at 150, 250, 350, and 450 °C in an atmospheric environment for 3 h and labeled as RA. The samples' UV−vis absorption spectra, plots of $(\alpha h\nu)^2$ vs $(h\nu)$, and I−V curves are shown in parts a−c of Figure 8, respectively. Interestingly, compared with the 24h-R:TNAs, the RA samples' absorption edges gradually shift to the ultraviolet light region and the band gaps widen again with the increase of reannealing temperature. The direct band gap energies of 24h-R:TNAs and RA are also
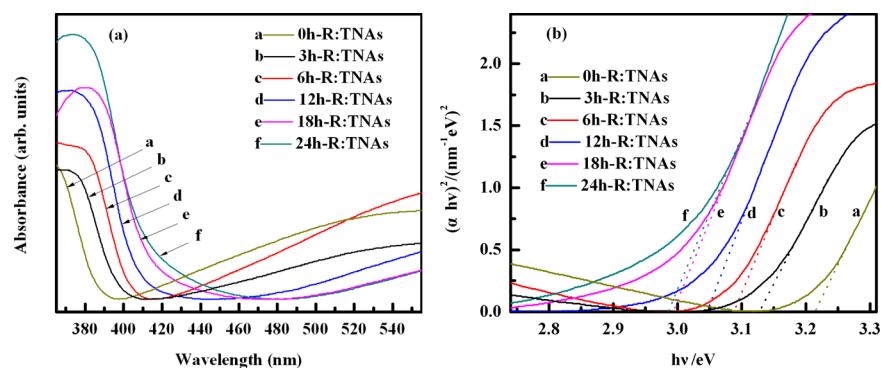
Figure 6. (a) UV−vis absorption spectra of *t*-R:TNAs synthesized at different reduction times of 0, 3, 6, 12, 18, and 24 h (curves a−f). (b) Plots of $(\alpha h\nu)^2$ vs $(h\nu)$ for the same samples.
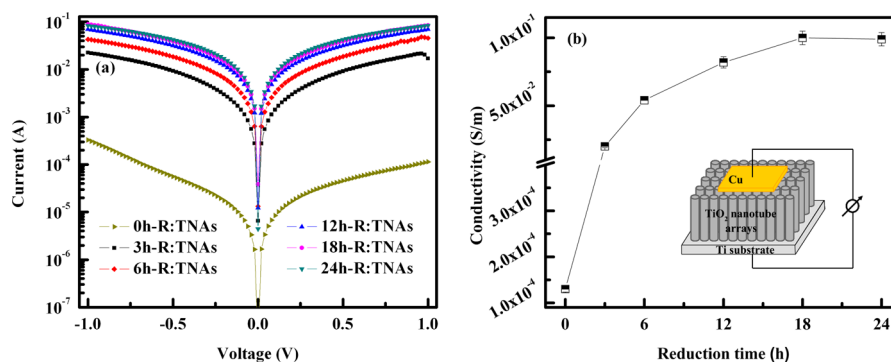

Figure 7. (a) *I−V* characteristics of the *t*-R:TNAs obtained at different reduction times. (b) Specific conductivity as a function of reduction time; inset: a simplified sketch of the 2-point measurement arrangement and the model for the calculation of conductivity.
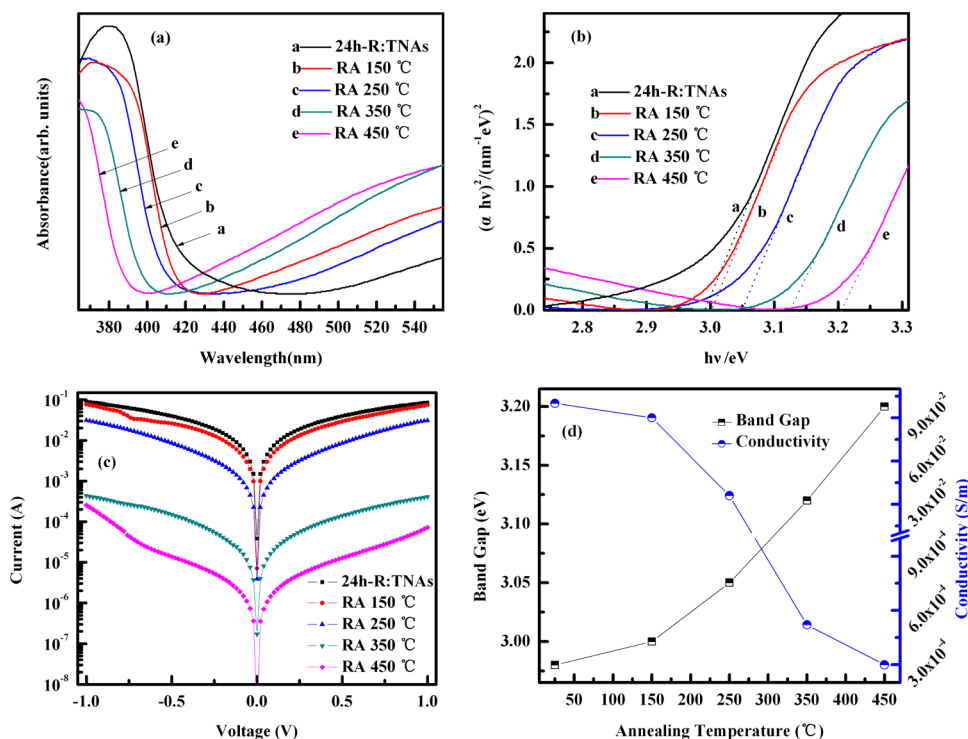

Figure 8. To test the thermal stability of oxygen vacancies, the 24h-R:TNAs is reannealed at 150, 250, 350, and 450 °C in an atmospheric environment for 3 h: (a, b, c) representing the UV−vis absorption spectra, plots of $(\alpha h\nu)^2$ vs $(h\nu)$, and *I−V* curves of the samples, respectively; (d) the corresponding variations of the band gap and conductivity with reannealed temperature (25 °C, 24h-R:TNAs).

estimated using the same method, and the results are shown in Figure 8d. Such phenomena indicate that once the 24h-

R:TNAs are reannealed in air, oxygen vacancies are filled with oxygen atoms. In addition, it is also found that the slightly
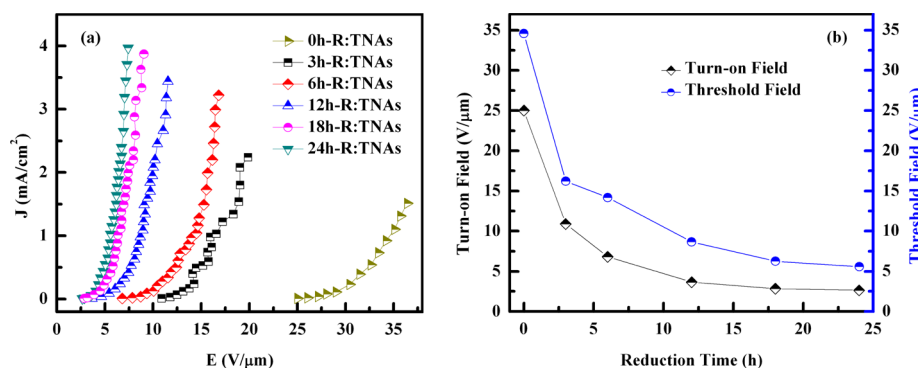
20629

dx.doi.org/10.1021/am503379y | *ACS Appl. Mater. Interfaces* 2014, 6, 20625−20633

Figure 9. (a) Emission current density (J) vs the applied field (E) curves of the t-R:TNAs with NaBH$_4$ treatment at various reduction times at 30 °C. (b) Dependence of turn-on and threshold field on the reduction time.

lower current fluctuated through the 150 and 250 °C annealed samples, compared with the current of the as-prepared 24h-R:TNAs in Figure 8c. As derived from the I−V data in Figure 8d, the TNAs conductivity decreases by 1.1 and 2.8 times after 150 and 250 °C annealing, respectively, implying the partial oxygen vacancies in TNAs are replaced by oxygen atoms. More importantly, compared with 0h-R:TNAs, the conductivity of the annealed TNAs is still much higher, revealing that part of the oxygen vacancies remain stable up to 250 °C. However, after >350 °C annealing, it shows a drastic decrease in current compared with the 24h-R:TNAs, and the samples' conductivity decreases to close to that of the 0h-R:TNAs, suggesting that all of the oxygen vacancies are replaced by oxygen atoms in TNAs. These phenomena indicate that the thermal stability of oxygen vacancies is relatively stable in a certain temperature range.

The FE properties of the t-R:TNAs are investigated and the corresponding current density versus electric field ($J−E$) curves are expressed in Figure 9a. The turn-on and threshold field are defined as the electric field at an emission current density of 10 μA/cm^2 and 1.0 mA/cm^2, respectively.[9,29] For the 0h-R:TNAs, the turn-on field is 25.01 V/μm and the threshold field is 34.59 V/μm. In contrast, for R:TNAs synthesized at different reduction times of 3, 6, 12, 18, and 24 h, the turn-on fields are 10.89, 6.81, 3.66, 2.85, and 2.65 V/μm, respectively, and the corresponding threshold fields are 16.22, 14.19, 8.66, 6.26, and 5.58 V/μm, as shown in Figure 9b. The FE performances of t-R:TNAs are strongly dependent on the reduction time. Moreover, it is worth notice that the turn-on fields and threshold fields continuously decrease, which is because the amount of the oxygen vacancy continuously increases with the increase of reduction time. If the reduction time is further extended up to 30 h, the results show that the FE properties of R:TNAs prepared at 30 h have no obvious change compared with the 24h-R:TNAs. As listed in Table 2, it is clearly seen that the turn-on and threshold field of 24h-R:TNAs are smaller than those of most of the TiO$_2$ nanostructure based FE devices, which are very promising for their practical applications in FE. In addition, the FE current density of 24h-R:TNAs can reach 3.5 mA/cm^2 at 7.2 V/μm.

The FE features are researched by the Fowler−Nordheim (F−N) equation,[35]

$$\ln(J/E^2) = \ln(A\beta^2/\varphi) + (-B\varphi^{3/2}/\beta)(1/E) \qquad (2)$$

where J, E, φ, and β are the current density, applied electric field, actual work function, and so-called field enhancement factor that is related to the geometry morphology of emitters and the testing distance between cathode and anode. A (1.56 ×

Table 2. Comparison of the Turn-on and Threshold Fields between the Present 24h-R:TNAs and the Recent Reports in the Literature for Other TiO$_2$ Based Nanostructures

emitters	morphology	turn-on field (V/μm)	threshold field (V/μm)	reference
TiO$_2$	nanotubes	7.8		30
TiO$_2$	ridged nanotubes	17.2		1
TiO$_2$	nanowires	4.1	11.5	31
TiO$_2$	nanotips	8.6	12.8	32
TiO$_{2-x}$	nanoplatelets		4.1	33
N-doped TiO$_2$	nanotubes	2.94	6.47	34
C-doped TiO$_2$	nanotubes	5.0		13
Fe-doped TiO$_2$	nanotubes	12		14
hydrogenated TiO$_2$	nanotubes	1.75	4.12	9
24h-R:TNAs	nanotubes	2.65	5.58	this work

10^{-10} A eV V^{-2}) and B (6.83 × 10^3 eV$^{-3/2}$ V μm^{-1}) are constants. As seen in Figure 10a, by a close observation of the data, all the samples have a poor linearity feature from the F−N plots. This is mainly due to the fact that the F−N theory is strictly effective for metal materials. As to wide band gap n-type semiconductors like TiO$_2$, the $J−E$ relationship could be amended as below,[36,37]

$$J = A(\beta^2 E^2/\varphi) \exp\{(-B\varphi^{3/2}/\beta)(1/E)\}$$
$$\exp\{(-\Delta W^S - \Delta W^P)/2kT\} \qquad (3)$$

where ΔW^P is the decrease of surface barrier potential for semiconductor nanostructures owing to field penetration, ΔW^S is the increase of surface barrier potential due to surface states, k is Boltzmann's constant, and T is the testing temperature. Because of the competition of ΔW^P and ΔW^S, the electrons will emit at different states with the changing of applied electric field intensities, where electrons can only be emitted beyond their critical field.[9,37] Therefore, F−N plots of samples show a nonlinear behavior. This nonlinear behavior also has been observed in the nitrogen-doped and hydrogenated TNAs. Even so, it makes sense to compare with the effective work function (φ_{eff}), defined as $\varphi_{\text{eff}} = \varphi/\beta^{2/3} = (-k/B)^{2/3}$, where k is the slope of the F−N plots.[35,37] If the effective work function is lower, a diminutive turn-on field and larger current density can be observed. The φ_{eff} of 0h-R:TNAs is calculated to be 0.145 eV, while the values of t-R:TNAs obtained at 3, 6, 12, 18, and 24 h, as shown in Figure 10b, can be calculated to be 0.060, 0.037,
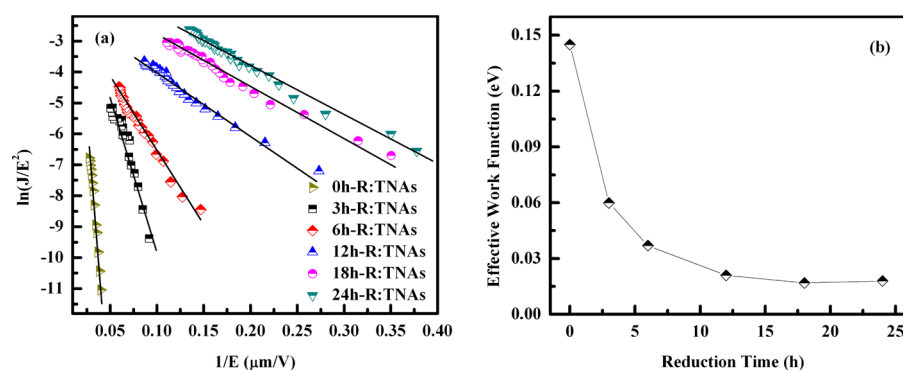
Figure 10. (a) F−N plots of *t*-R:TNAs at various reduction times. (b) Corresponding variation of the effective work function with reduction time.

0.021, 0.017, and 0.017 eV, respectively, by using the F−N plot. Among the range of treatment time in this research, the φ_{eff} continually decreases with the increase of the treatment time, which is also explained because the oxygen vacancies gradually increase and have a tendency to saturate.

Distinctly, the FE properties of *t*-R:TNAs are dramatically improved, which attribute to the fact that the changing of the band structure due to the surface morphology of specimens (Figure 2a−f) and the testing distance between cathode and anode (50 μm) have not altered in this work. As seen in Figure 10b, the φ_{eff} of *t*-R:TNAs decrease markedly with the increasing of reduction time. Theoretically speaking, the effective work function of field emitters is related to their field enhancement factor and actual work function. The studies have found that the reduction treatment can increase the oxygen vacancy concentration in the TNAs.[21,23] The introduced oxygen vacancies act as donor states and locate at about 0.75−1.18 eV below the conduction band.[20] These donor states will be ionized; therefore, it will give rise to the upward Fermi level shift and enlarge the density of carriers, as shown in Figure 11.
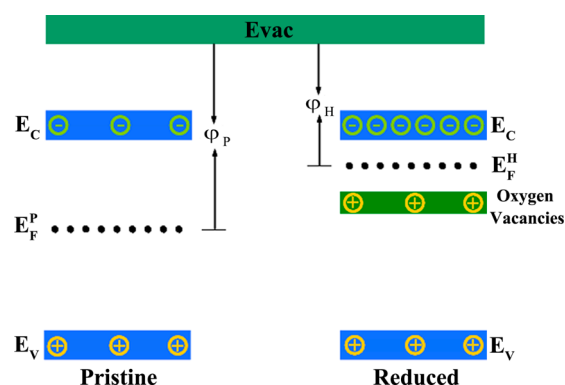

Figure 11. Schematic energy-level change of pristine TNAs modified by introduced oxygen vacancies, illustrating how oxygen vacancy levels shift the Fermi level (E_F) and decrease actual work function (φ). E_F^P and E_F^H are the Fermi levels of the pristine TNAs and R:TNAs. Evac, E_V, and E_C are the vacuum level, valence band, and conduction band, respectively.

Consequently, the increased oxygen vacancy concentration leads to the modification of energy band structure, resulting in reducing the actual work function and, thus, improving the FE properties of TNAs.

On the other hand, the improved conductivity is another factor to be considered. The enhancement of conductivity will make the electronic transmissions become easy from the nanotubes to emission sites and diminish the voltage drop along the TNAs so that the effective field at the emission site would be augmented, which is favorable for FE.[9] Therefore, the alterations of band structure, including the decreased φ_{eff} and increased conductivity, result in the enhanced FE properties such as low turn-on field and high emission current density.

The long-term stability and repeatability of the field emitters are also important parameters for practical application. Figure 12a shows the stability feature of 24h-R:TNAs at 1.50 mA/cm^2 (constant electric field of 6.18 V/μm) over the duration of 480 min. In the initial 100 min stage, the emission current density displays a slight enhancement and then tends to stabilize with only a slight change in the remaining 380 min. The fluctuant current density could be attributed to the cleaning effect on the emitter surface because of bombardment and ion emission.[9,21,29] Once the surfaces of R:TNAs are cleaned by the ion bombardment process, stable FE current density can be achieved. In addition, the superior repeatability of FE is further demonstrated in a cyclic electric field experiment. We also carry out the cyclic measurements of FE of 24h-R:TNAs. The FE repeatability of the sample is researched by modulating the strength of the applied field from 0 to 8.0 V/μm. After cycling the electric field two times, as shown in Figure 12b, the J−E curves are repeatable within the range of experimental error under identical conditions. The results indicate that the samples have a stable and homogeneous electron emission. That is to say, the R:TNAs show remarkable electron emission stability and repeatability, which leaves no doubt that they are promising field emitters for practical application.

■ CONCLUSIONS

In this work, the R:TNAs were prepared via a straightforward liquid-phase reduction strategy using NaBH$_4$ as the reductive agent. By controlling and adjusting the reduction time over the range of 0−24 h, the reduction treatment can introduce oxygen vacancies, resulting in elevating the Fermi level, improving the conductivity, and reducing the effective work function of the TNAs. All of the above-mentioned factors result in enhanced FE performances. Notably, the 24h-R:TNAs show a low turn-on field (~2.65 V/μm) and excellent FE stability and repeatability. More importantly, the thermal stability of oxygen vacancies is investigated by analyzing the UV−vis absorption spectra and I−V curves of the RA samples, indicating that it is relatively stable in a certain temperature range. These results unambiguously point out that the R:TNAs are promising flat panel displays and electron emitter devices.
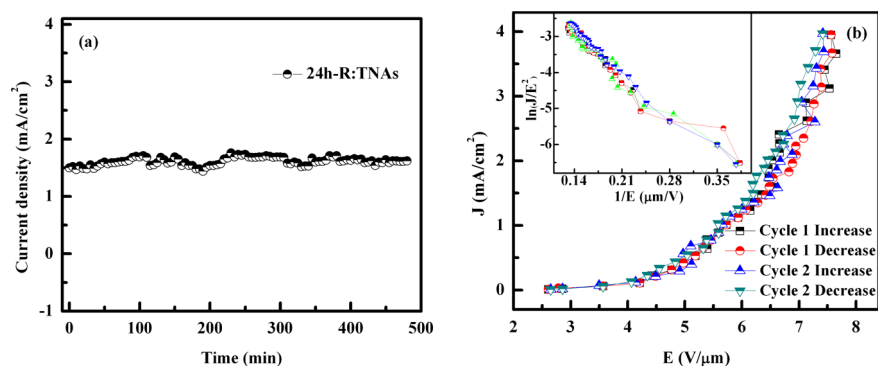
Figure 12. Stability of FE from 24h-R:TNAs: (a) measurement conducted at a constant electric field of 6.18 V/μm; (b) cyclic FE measurement. The inset in (b) is the corresponding F−N plots.

■ AUTHOR INFORMATION

Corresponding Author

*Tel.: +86-18509311337; fax: +86-09317971503. E-mail: cwwang@nwnu.edu.cn.

Notes

The authors declare no competing financial interest.

■ ACKNOWLEDGMENTS

■ REFERENCES

(1) Xu, X.; Tang, C.; Zeng, H.; Zhai, T.; Zhang, S.; Zhao, H.; Bando, Y.; Golberg, D. Structural Transformation, Photocatalytic, and Field-Emission Properties of Ridged TiO$_2$ Nanotubes. *ACS Appl. Mater. Interfaces* **2011**, *3*, 1352−1358.

(2) Wang, C. W.; Chen, J. B.; Wang, L. Q.; Kang, Y. M.; Li, D. S.; Zhou, F. Single Crystal TiO$_2$ Nanorods: Large-Scale Synthesis and Field Emission. *Thin Solid Films* **2012**, *520*, 5036−5041.

(3) Guo, R. S.; Wang, C. W.; Chen, J. B.; Wang, J.; Wang, L. Q.; Liu, W. M. Field Emission from TiO$_2$/Ti Nanotube Arrays with Different Morphologies. *Phys. B* **2010**, *405*, 4682−4686.

(4) Fang, X.; Yan, J.; Hu, L.; Liu, H.; Lee, P. S. Thin SnO$_2$ Nanowires with Uniform Diameter as Excellent Field Emitters: A Stability of More Than 2400 minutes. *Adv. Funct. Mater.* **2012**, *22*, 1613−1622.

(5) Sun, X.; Liu, W.; Ouyang, D. Synthesis of Iron Oxide Nanoneedles and Their Field Emission Properties. *J. Alloys Compd.* **2009**, *478*, 38−40.

(6) Chu, F. H.; Huang, C. W.; Hsin, C. L.; Wang, C. W.; Yu, S. Y.; Yeh, P. H.; Wu, W. W. Well-Aligned ZnO Nanowires with Excellent Field Emission and Photocatalytic Properties. *Nanoscale* **2012**, *4*, 1471−1475.

(7) Wang, X. P.; Wang, L. J.; Liu, X. F.; Yang, C.; Jing, L. W.; Pan, X. F.; Li, S. K. The Synthesis of Vertically Oriented Carbon Nanosheet-Carbon Nanotube Hybrid Films and Their Excellent Field Emission Properties. *Carbon* **2013**, *58*, 170−174.

(8) Lee, D. H.; Lee, J. A.; Lee, W. J.; Kim, S. O. Flexible Field Emission of Nitrogen-Doped Carbon Nanotubes/Reduced Graphene Hybrid Films. *Small* **2011**, *7*, 95−100.

(9) Zhu, W. D.; Wang, C. W.; Chen, J. B.; Li, D. S.; Zhou, F.; Zhang, H. L. Enhanced Field Emission from Hydrogenated TiO$_2$ Nanotube Arrays. *Nanotechnology* **2012**, *23*, 455204.

(10) Liao, A. Z.; Zhu, W. D.; Chen, J. B.; Zhang, X. Q.; Wang, C. W. Vertically Aligned Single-Crystalline Ultra-Thin CuO Nanosheets: Low-Temperature Fabrication, Growth Mechanism, and Excellent Field Emission. *J. Alloys Compd.* **2014**, *609*, 253−261.

(11) Alivov, Y.; Klopfer, M.; Molloi, S. Enhanced Field Emission from Clustered TiO$_2$ Nanotube Arrays. *Appl. Phys. Lett.* **2011**, *99*, 063104.

(12) Liu, G.; Li, F.; Wang, D. W.; Tang, D. M.; Liu, C.; Ma, X.; Lu, G. Q.; Cheng, H. M. Electron Field Emission of a Nitrogen-Doped TiO$_2$ Nanotube Array. *Nanotechnology* **2008**, *19*, 025606.

(13) Wang, L. Q.; Wang, C. W.; Chen, J. B.; Guo, R. S.; Zhou, F.; Liu, W. M. Electron Field Emission from the Carbon-Doped TiO$_2$ Nanotube Arrays. *Thin Solid Films* **2011**, *519*, 8173−8177.

(14) Wang, C. C.; Wang, K. W.; Perng, T. P. Electron Field Emission from Fe-Doped TiO$_2$ Nanotubes. *Appl. Phys. Lett.* **2010**, *96*, 143102.

(15) Kang, H. W.; Yeo, J.; Hwang, J. O.; Hong, S.; Lee, P.; Han, S. Y.; Lee, J. H.; Rho, Y. S.; Kim, S. O.; Ko, S. H.; Sung, H. J. Simple ZnO Nanowires Patterned Growth by Microcontact Printing for High Performance Field Emission Device. *J. Phys. Chem. C* **2011**, *115*, 11435−11441.

(16) Zhou, X. T.; Lin, T. H.; Liu, Y. H.; Wu, C. X.; Zeng, X. Y.; Jiang, D.; Zhang, Y. A.; Guo, T. L. Structural, Optical, and Improved Field-Emission Properties of Tetrapod-Shaped Sn-Doped ZnO Nanostructures Synthesized via Thermal Evaporation. *ACS Appl. Mater. Interfaces* **2013**, *5*, 10067−10073.

(17) Greiner, M. T.; Chai, L.; Helander, M. G.; Tang, W. M.; Lu, Z. H. Transition Metal Oxide Work Functions: The Influence of Cation Oxidation State and Oxygen Vacancies. *Adv. Funct. Mater.* **2012**, *22*, 4557−4568.

(18) Kang, Q.; Cao, J.; Zhang, Y.; Liu, L.; Xu, H.; Ye, J. Reduced TiO$_2$ Nanotube Arrays for Photoelectrochemical Water Splitting. *J. Mater. Chem. A* **2013**, *1*, 5766−5774.

(19) Kitada, A.; Hasegawa, G.; Kobayashi, Y.; Kanamori, K.; Nakanishi, K.; Kageyama, H. Selective Preparation of Macroporous Monoliths of Conductive Titanium Oxides Ti$_n$O$_{2n-1}$ (n = 2, 3, 4, 6). *J. Am. Chem. Soc.* **2012**, *134*, 10894−10898.

(20) Zhang, H. X.; Zhao, M.; Jiang, Q. Effect of Oxygen Vacancies on Electronic Structures and Field Emission Properties of TiO$_2$ Nanotubes: A Density-Functional Theory Investigation. *Appl. Phys. Lett.* **2013**, *103*, 023111.

(21) Zhu, W. D.; Wang, C. W.; Chen, J. B.; Zhang, X. Q. Low Temperature Synthesis of Reduced Titanium Oxide Nanotube Arrays: Crystal Structure Transformation and Enhanced Field Emission. *Mater. Res. Bull.* **2014**, *50*, 79−84.

(22) Walsh, F. C.; Wills, R. G. A. The Continuing Development of Magnéli Phase Titanium Sub-Oxides and Ebonex Electrodes. *Electrochim. Acta* **2010**, *55*, 6342−6351.

(23) Xing, M.; Fang, W.; Nasir, M.; Ma, Y.; Zhang, J.; Anpo, M. Self-Doped Ti^{3+}-Enhanced TiO$_2$ Nanoparticles with a High-Performance Photocatalysis. *J. Catal.* **2013**, *297*, 236−243.

(24) Patterson, A. The Scherrer Formula for X-Ray Particle Size Determination. *Phys. Rev.* **1939**, *56*, 978−982.

(25) Lu, X.; Wang, G.; Xie, S.; Shi, J.; Li, W.; Tong, Y.; Li, Y. Efficient Photocatalytic Hydrogen Evolution over Hydrogenated ZnO Nanorod Arrays. *Chem. Commun.* **2012**, *48*, 7717−7719.

(26) Wang, D.; Liu, L.; Zhang, F.; Tao, K.; Pippel, E.; Domen, K. Spontaneous Phase and Morphology Transformations of Anodized Titania Nanotubes Induced by Water at Room Temperature. *Nano Lett.* **2011**, *11*, 3649−3655.

(27) Wang, J.; Wang, C. W.; Li, Y.; Liu, W. M. Optical Constants of Anodic Aluminum Oxide Films Formed in Oxalic Acid Solution. *Thin Solid Films* **2008**, *516*, 7689−7694.

(28) Hu, Y. H. A Highly Efficient Photocatalyst-Hydrogenated Black TiO$_2$ for the Photocatalytic Splitting of Water. *Angew. Chem., Int. Ed.* **2012**, *51*, 12410−12412.

(29) Zhang, X. Q.; Chen, J. B.; Zhu, W. D.; Wang, C. W. Enhanced Field Emission from Hydrogenated SnO$_2$ Nanoparticles Embedded in TiO$_2$ Film on Fluorinated Tin Oxide Substrate. *J. Vac. Sci. Technol., B* **2014**, *32*, 021808.

(30) Chen, J. B.; Wang, C. W.; Ma, B. H.; Li, Y.; Wang, J.; Guo, R. S.; Liu, W. M. Field Emission from the Structure of Well-Aligned TiO$_2$/Ti Nanotube Arrays. *Thin Solid Films* **2009**, *517*, 4390−4393.

(31) Huo, K.; Zhang, X.; Fu, J.; Qian, G.; Xin, Y.; Zhu, B.; Ni, H.; Chu, P. K. Synthesis and Field Emission Properties of Rutile TiO$_2$ Nanowires Arrays Grown Directly on a Ti Metal Self-Source Substrate. *J. Nanosci. Nanotechnol.* **2009**, *9*, 3341−3346.

(32) Liang, J.; Zhang, G. TiO$_2$ Nanotip Arrays: Anodic Fabrication and Field-Emission Properties. *ACS Appl. Mater. Interfaces* **2012**, *4*, 6053−6061.

(33) Raut, N. C.; Mathews, T.; Panda, K.; Sundaravel, B.; Dash, S.; Tyagi, A. K. Enhancement of Electron Field Emission Properties of TiO$_{2−x}$ Nanoplatelets by N-Doping. *RSC Adv.* **2012**, *2*, 812−815.

(34) Wang, C. W.; Zhu, W. D.; Chen, J. B.; Hou, X.; Zhang, X. Q.; Li, Y.; Wang, J.; Zhou, F. Low-Temperature Ammonia Annealed TiO$_2$ Nanotube Arrays: Synergy of Morphology Improvement and Nitrogen Doping for Enhanced Field Emission. *Thin Solid Films* **2014**, *556*, 440−446.

(35) Forbes, R. G. Simple Good Approximations for the Special Elliptic Functions in Standard Fowler−Nordheim Tunneling Theory for a Schottky−Nordheim Barrier. *Appl. Phys. Lett.* **2006**, *89*, 113122.

(36) Ahmed, S. F.; Das, S.; Mitra, M. K.; Chattopadhyay, K. K. Effect of Temperature on the Electron Field Emission from Aligned Carbon Nanofibers and Multiwalled Carbon Nanotubes. *Appl. Surf. Sci.* **2007**, *254*, 610−615.

(37) Antony, R. P.; Mathews, T.; Panda, K.; Sundaravel, B.; Dash, S.; Tyagi, A. K. Enhanced Field Emission Properties of Electrochemically Synthesized Self-Aligned Nitrogen-Doped TiO$_2$ Nanotube Array Thin Films. *J. Phys. Chem. C* **2012**, *116*, 16740−16746.